Asian Journal of Chemistry; Vol. 37, No. 12 (2025), 3055-3064
ASIAN JOURNAL OF CHEMISTRY
https://doi.org/10.14233/ajchem.2025.34683

Enhanced Photocatalytic Degradation of Eosin Yellow Dye using Fe_3O_4 Nanoparticles from *S. prostrata* Leaf Extract and their Cytotoxicity against MCF-7 Cell Line

MURIPINTI BALAKRISHNA[1,2], GOPI MAMIDI[2,*], SATHISH MOHAN BOTSA[3] and G. PAVAN KUMAR[4]

[1]AU-TDR Hub, Andhra University, Visakhapatnam-530003, India
[2]Department of Chemistry, Dr. V.S. Krishna Government Degree College (A), Visakhapatnam-530022, India
[3]Bio Enviro Chemical Solutions, Visakhapatnam-530017, India
[4]Department of Physics, St. Joseph's College for Women (A), Visakhapatnam-530004, India

*Corresponding authors: E-mail: iitmgopi@gmail.com

Received: 11 August 2025 *Accepted*: 8 October 2025 *Published online*: 30 November 2025 AJC-22195

In this study, superparamagnetic iron oxide nanoparticles (SPR-Fe_3O_4 NPs) were successfully synthesized *via* green route using *Suaeda prostrata* leaf extract as a natural reducing and stabilizing agent. The phytochemicals in the extract facilitated the formation of uniformly distributed, crystalline nanoparticles under eco-friendly conditions. Comprehensive characterization using XRD, FTIR, UV-Vis, SEM-EDX, HRTEM, XPS and VSM techniques confirmed the structural integrity, surface morphology, elemental composition, magnetic properties and functional groups involved in the bioreduction process. The average crystalline size of SPR-Fe_3O_4 NPs is 21.3 nm, exhibits superparamagnetic nature (14999.92 Oe) and characteristic type IV isotherm with a prominent H3-type hysteresis loop suggests monolayer-multilayer adsorption. The SPR-Fe_3O_4 NPs exhibited excellent photocatalytic performance in the degradation of eosin yellow (EY) dye under visible light, with degradation efficiency influenced by catalyst dosage (50 mg) and dye concentration (10 mg/L) in 80 min. Kinetic studies indicated a pseudo-first-order reaction mechanism. Notably, the catalyst maintained over 85% degradation efficiency after five consecutive cycles, with minimal structural changes as confirmed by XRD analysis, demonstrating outstanding reusability and stability. These results confirm that SPR-Fe_3O_4 NPs exhibit concentration-dependent cytotoxic activity against MCF-7 cells (128.67 mean), making them potentially useful in cancer nanomedicine applications, particularly in targeted therapy or drug delivery systems.

Keywords: Fe_3O_4 Nanoparticles, Leaf extract, Eosin yellow dye, Visible light irradiation, Anticancer activity.

INTRODUCTION

Organic dye pollutants represent a major source of environmental contamination, significantly contributing to the degradation of aquatic and terrestrial ecosystems. Industrial effluents, particularly from textile, brewery, paper, food and cosmetic industries, are the primary sources of these dye-laden wastewaters [1]. Among the various dyes, eosin yellow (EY), an anionic xanthene dye, is extensively utilized in pharmaceuticals, ink formulation and textile manufacturing. However, its widespread discharge into water bodies poses significant ecological and health risks. Based on mechanism, it is well reported that this dye disrupts the protein–protein interactions, resulting in the skin irritation and exhibits genotoxicity in humans, necessitating its effective removal from wastewater [2,3]. The persistence of synthetic dyes like EY, due to aromatic structural complex and resistance to biodegradation, limits the efficiency of conventional treatments such as coagulation, filtration and adsorption, which often fail to achieve complete mineralization and generate secondary waste. Consequently, innovative, cost-effective and environmentally benign strategies are urgently needed.

Nanotechnology has emerged as a promising solution, with metal oxide nanoparticles exhibiting unique optical, electronic and surface properties and the ability to generate the reactive oxygen species (ROS) under light, enabling effective dye degradation [4-6]. Magnetic iron oxide nanoparticles (IONPs), particularly magnetite (Fe_3O_4), are widely used due to their multifunctionality, biocompatibility, high surface area, thermal and pH stability and recyclability [7-9]. Their magnetic properties facilitate easy separation and reuse, making them suitable for wastewater treatment, among other biomedical applications such as drug delivery, MRI contrast, biosensing and protein purification [10]. Conventional

IONPs synthesis often involves toxic solvents and stabilizers, prompting interest in green synthesis methods using non-toxic precursors, benign solvents, and natural reducing agents from plant or microbial sources, which minimize environmental impact while being cost-effective and scalable [11-13].

Plant extracts, rich in polyphenols, alkaloids and flavonoids, can act as reducing and capping agents, producing stable, size-controlled nanoparticles [14]. *Suaeda maritima* (L.) Dumort., a halophytic Amaranthaceae species known locally as Elakura, grows in coastal salt flats and tidal marshes and is used as food and fodder. Traditionally, it has been applied in folk medicine for liver ailments and exhibits antioxidant, hepatoprotective, and antimicrobial properties [15].

Our study aimed to develop eco-friendly Fe_3O_4 nanoparticles through a sustainable green synthesis approach using *Suaeda prostrata* leaf (SPR) extract as both a reducing and stabilizing agent. The synthesized SPR-Fe_3O_4 NPs were thoroughly characterized by XRD, FTIR, SEM, HRTEM, UV-Vis and VSM to confirm their crystallinity, morphology, optical and magnetic properties. Under optimized conditions, the SPR-Fe_3O_4 NPs efficiently degraded eosin yellow (EY) dye, demonstrating their potential as effective nanocatalysts for wastewater remediation. Reusability studies further confirmed their structural stability and sustained catalytic performance, emphasizing their recyclability and suitability for green wastewater treatment. Beyond environmental applications, the magnetic properties of SPR-Fe_3O_4 NPs were explored for biomedical purposes and their anticancer potential was evaluated against breast cancer (MCF-7) cell lines, highlighting their multifunctional applicability.

EXPERIMENTAL

Fresh *Suaeda prostrata* leaves were collected from the vicinity of the port area in Visakhapatnam, Andhra Pradesh, India (17º44′25″N, 83º19′15″E). Ferric chloride ($FeCl_3$) with 98% of AR grade and other chemicals were procured from Merck, India and used without further purification. Distilled water was employed in all experiments.

Preparation of *Suaeda prostrata* leaf extract: Fresh *Suaeda prostrata* leaves were carefully washed with tap water followed by thorough rinsing with distilled water to remove any surface contaminants. The cleaned leaves were dried under shade until completely dehydrated. The dried leaves were then ground into a fine powder using a household grinder. A quantity of 2 g of the powdered material was added to 100 mL of distilled water in a 250 mL glass beaker. The mixture was heated at 70 ºC for 2 h using a hot plate, resulting in the formation of a brown coloured solution. This extract was filtered using Whatman No. 1 filter paper to remove any solid residues. The filtrate was then stored at 4 ºC for further use.

Synthesis of *S. prostrata*-mediated α-Fe_2O_3 NPs: To synthesize *S. prostrata* leaves (SPR) extract Fe_3O_4 NPs, 200 mL of 0.05 N $FeCl_3$ solution was taken in a 500 mL beaker and stirred for 5 min to ensure homogeneity. Subsequently, 50 mL of the prepared *S. prostrata* leaf extract was added to the solution. The beaker was covered with aluminum foil to minimize evaporation during the reaction. The mixture was then stirred at 70 ºC for 3 h at a constant speed of 500 rpm, leading to the formation of a brown-coloured suspension. The suspension was left undisturbed for 6 h in dark to complete the reaction. The resulting brown precipitate was filtered and the solid was dried in a hot air oven at 60 ºC for 6 h. Finally, the dried material was ground into a fine powder using a mortar and pestle, rendering it ready for subsequent characterization.

Characterization: A range of advanced analytical techniques was employed to characterize the green-synthesized SPR-Fe_3O_4 NPs in terms of their structural, morphological, optical and magnetic properties. X-ray diffraction (XRD) analysis using a D8 Bruker Kappa Apex II diffractometer confirmed the crystalline nature and phase purity of the nanoparticles. The functional groups involved in the bioreduction and stabilization were identified by FTIR spectroscopy (Shimadzu IR Prestige2) in the range of 4000-400 cm^{-1} using KBr pellets. Optical properties were examined *via* UV-Vis spectroscopy (LabIndia UV-3092) in the 200-800 nm range. Surface morphology and elemental composition were investigated using SEM (JEOL 6390LA) combined with EDX analysis. Detailed particle size and crystallinity were assessed by HRTEM (JEOL JEM-2100) at 200 kV. XPS (Axis Ultra) was used to determine the oxidation states of elements, while magnetic properties were studied at room temperature using a VSM (Lakeshore 7410) under applied magnetic fields.

Photocatalytic experiments: The photocatalytic efficiency of the green-synthesized SPR-Fe_3O_4 nanoparticles was investigated for the degradation of eosin yellow (EY) dye under visible light illumination [6]. In brief, 50 mL of EY dye solution (10 mg/L) was combined with 50 mg of SPR-Fe_3O_4 nanocatalyst. To establish adsorption–desorption equilibrium, the mixture was stirred magnetically in dark for 30 min. Following this equilibration period, the suspension was exposed to visible light using a 400 W metal halide lamp, simulating indoor sunlight conditions. All experiments were performed at room temperature. At defined time intervals during irradiation, aliquots of the reaction mixture were withdrawn to monitor the degradation progress. These samples were immediately centrifuged at 4000 rpm to separate the photocatalyst from the solution. The remaining concentration of EY dye was determined by recording the absorbance at 509 nm using a UV-visible spectrophotometer. The photocatalytic degradation efficiency was calculated using a standard equation (eqn. 1):

$$\text{Degradation (\%)} = \frac{A_o - A_t}{A_o} \times 100 \quad (1)$$

where A_o is the initial absorbance of the dye solution and A_t is the absorbance at a given time t.

Anticancer activity: The cytotoxic potential of the test samples against the MCF-7 breast cancer cell line was assessed using the neutral red uptake (NRU) assay. MCF-7 cells were seeded in 96-well culture plates at a density of 5000-8000 cells per well and incubated for 24 h in Dulbecco's modified eagle medium (DMEM, AT149-1L) supplemented with 10% fetal bovine serum (FBS, HiMedia RM10432) and 1% antibiotic solution. The incubation was carried out at 37 ºC in a humidified atmosphere containing 5% CO_2. After 24 h, the spent medium was removed and replaced with fresh DMEM. Subsequently, 5 μL of test sample dilutions at varying

concentrations were added to the designated wells and the plates were incubated for another 24 h under the same conditions. Following the treatment period, 100 µL of Neutral Red solution (40 µg/mL in PBS) was added to each well and incubated for 1 h in a CO_2 incubator (Heal Force Smartcell, HF-90). After incubation, the dye-containing medium was discarded and the absorbed dye was extracted using 100 µL of NRU destaining solution per well. The absorbance was measured at 550/660 nm using a microplate reader to quantify cell viability.

RESULTS AND DISCUSSION

The formation of SPR-Fe_3O_4 NPs was accomplished *via* a green synthesis route utilizing *S. prostrata* leaf extract, which served as a natural reducing, capping and stabilizing agent [3]. In a typical procedure, an aqueous solution of $FeCl_3$ was mixed with the freshly prepared plant extract under constant stirring. The bioactive compounds present in the extract, such as phenolics, flavonoids, alkaloids and terpenoids, played a crucial role in reducing Fe^{3+} ions to Fe_3O_4 NPs and simultaneously capping the formed particles to prevent agglomeration. The reaction mixture was maintained at an elevated temperature (70 ºC) for several hours, facilitating the nucleation and controlled growth of the nanoparticles. A noticeable colour transition from pale yellow to dark brown-black was observed, indicating the formation of Fe_3O_4 NPs due to the surface plasmon resonance phenomenon. The plant extract not only eliminated the need for hazardous chemicals but also imparted bio-functional groups onto the nanoparticle surface, enhancing their stability and biocompatibility. This green synthesis approach offers a sustainable, cost-effective and environmentally benign alternative to conventional chemical methods for producing magnetic nanoparticles.

XRD spectral studies: The X-ray diffraction (XRD) patterns of the synthesized Fe_3O_4 NPs using *S. prostrata* leaves extract demonstrates a series of sharp and intense peaks, confirming the crystalline nature of the sample (Fig. 1). The major diffraction peaks were observed at 2θ values of 24.21º, 30.24º, 33.14º, 35.7º, 40.84º, 43.43º, 49.42º, 54.09º, 57.47º, 62.85º and 63.99º. These peak positions closely correspond to the characteristic reflections of iron oxide phases, particularly magnetite (Fe_3O_4) and maghemite (γ-Fe_2O_3), the JCPDS card No. 19-0629 for Fe_3O_4 [16] lists the prominent peaks at 2θ values around 30.1º (220), 35.5º (311), 43.1º (400), 53.5º (422), 57.0º (511) and 62.6º (440), which match well with the observed data. The average crystalline size of Fe_3O_4 NPs is found to be 21.3 nm as obtained from Debey-Scherrer's formula.

Morphology and elemental analysis: The surface morphology of the green-synthesized SPR-Fe_3O_4 NPs was investigated using SEM at different magnifications. Fig. 2a displays the SEM image revealing a dense, agglomerated surface with semi-spherical nanoparticle clusters. A few elongated rod-like or flake structures, likely phytochemical residues or anisotropic crystal growths, are also observed, suggesting incomplete decomposition of plant-based organic compounds during synthesis. This supports the role of the plant extract not only in reducing metal ions but also in capping and stabilizing the nanoparticles [17]. As shown in Fig. 2b, the SPR-Fe_3O_4 NPs exhibit a relatively uniform and highly porous surface morphology composed of aggregated nanosized grains. The porous structure and aggregation could be attributed to the magnetic interactions between the Fe_3O_4 cores as well as the organic moieties from the plant extract that may bridge adjacent particles. This morphology is favourable for catalytic applications due to increased surface area and active sites.

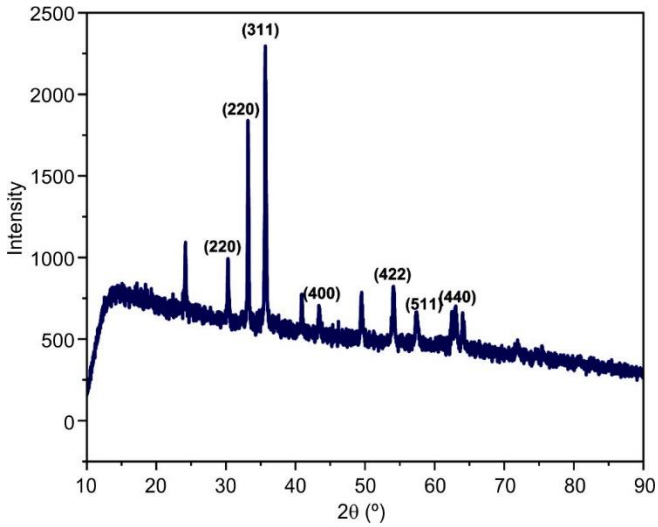

Fig. 1. XRD patterns of prepared Fe_3O_4 NPs using *S. prostrata* leaf extract

The elemental composition and distribution of the green synthesized nanoparticles were further confirmed by energy dispersive X-ray (EDX) spectroscopy and elemental mapping. Fig. 2c-d shows the EDX analysis with quantitative data revealing the presence of iron (Fe) and oxygen (O), with weight percentages of 68.29% and 31.71%, respectively. The corresponding atomic percentages were 38.32% for Fe and 61.68% for O, which is consistent with the stoichiometry of Fe_3O_4. The absence of other elemental signals confirms the purity of the synthesized nanoparticles and successful capping without any foreign metal contamination.

TEM analysis of Fe_3O_4 NPs synthesized using *S. prostrata* leaf extract provides comprehensive insight into their morphology, size and crystallinity. The low-magnification TEM image (Fig. 3a) reveals that the nanoparticles exhibit a quasi-spherical to irregular morphology with visible clustering. The particle sizes range between 10 to 50 nm and the observed agglomeration may be attributed to the magnetic nature of iron oxide as well as partial capping by phytochemicals from the leaf extract [3,17]. TEM image shows (Fig. 3b) more clearly defined individual nanoparticles with visible grain boundaries, suggesting their polycrystalline nature. The contrast and shape of the particles further support the formation of well-developed iron oxide nanostructures. These features are indicative of efficient nucleation and growth of nanoparticles during the green synthesis process. Fig. 3c highlights distinct lattice fringes, which confirm the crystalline structure of the nanoparticles. Although the interplanar spacing is not directly measured here, the presence of fringes is characteristic of crystalline phases such as hematite (α-Fe_2O_3) or magnetite (Fe_3O_4). This confirms that the nanoparticles are not amorphous and possess a defined atomic arrangement. The selected area electron diffraction (SAED) patterns (Fig. 3d) display well-defined diffraction spots arranged in concentric rings.

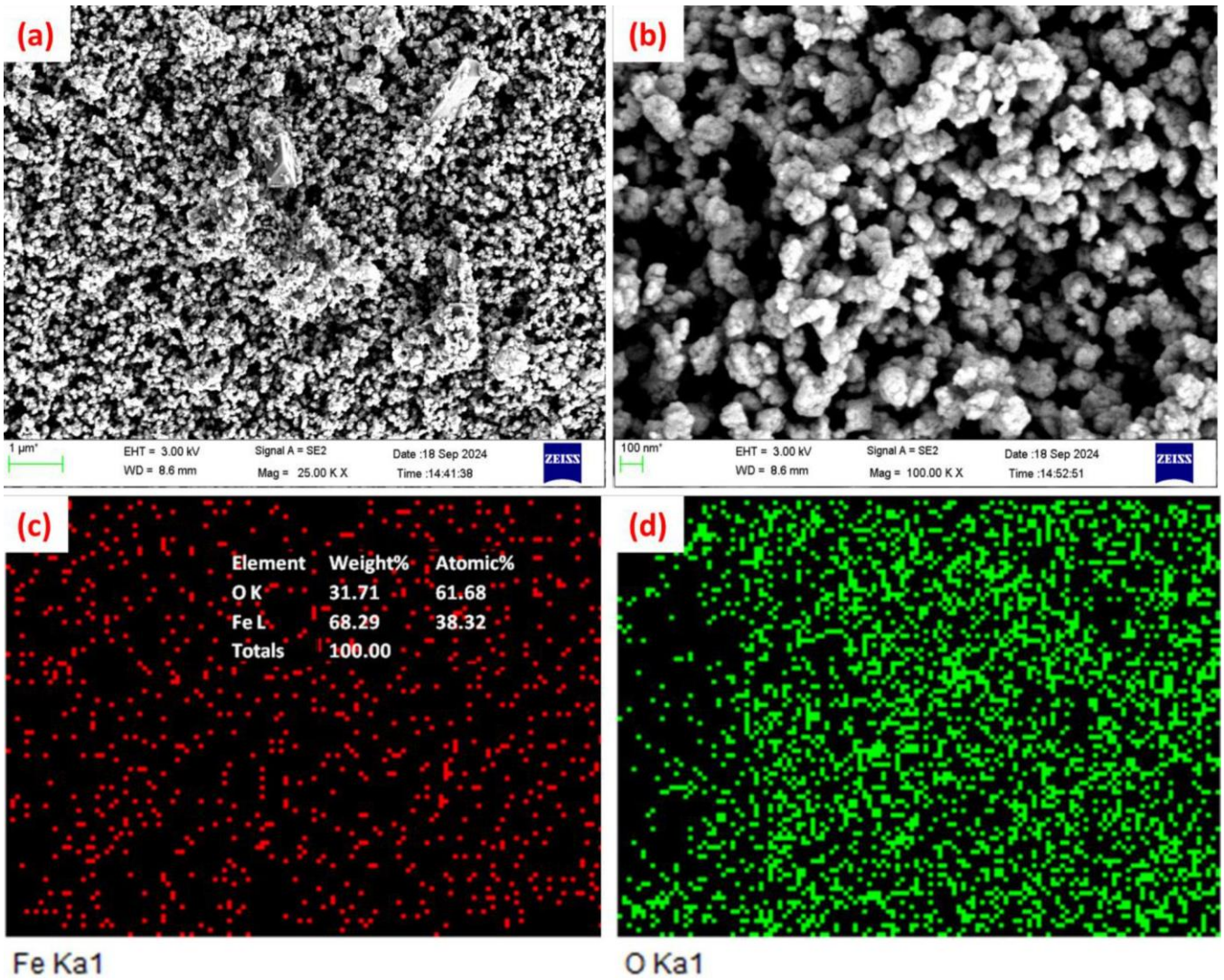

Fig. 2. (a,b) SEM and (c,d) EDX images of SPR-Fe_3O_4 NPs

This ring pattern is typical of polycrystalline materials and corresponds to different crystallographic planes of iron oxide. The sharpness and clarity of these rings further validate the crystalline purity of the synthesized nanoparticles and concurred with XRD results.

FTIR studies: The FTIR spectrum of Fe_3O_4 NPs synthesized with *S. prostrata* leaves extract displays key absorption bands corresponding to both the iron oxide core and capping organic groups (Fig. 4). The broad band near 3400 cm^{-1} (O-H *str.*) and peaks at 2920 cm^{-1} (C-H *str.*), 1740 cm^{-1} (C=O *str.*) and 1626 cm^{-1} (amide I or water bending) indicate the presence of phytochemicals from the extract. Notably, strong bands at 619 cm^{-1} and 490 cm^{-1} correspond to the Fe-O stretching vibrations, confirming the formation of iron oxide nanoparticles [16].

Optical studies: The UV-Vis absorption spectrum of a sample measured in the wavelength range of 200-800 nm (Fig. 5) exhibits a broad and strong absorbance in the UV region, with maximum absorbance values above 1.2 between approximately 250 nm and 600 nm. The absorbance gradually decreases beyond 600 nm and continues to decline towards 800 nm. This spectral profile is characteristic of Fe_3O_4 NPs, which typically display broad absorption in the UV-Visible range due to their electronic transitions and surface plasmon resonance effects. The high absorbance in the UV-visible regions suggests efficient light absorption, which is consistent with the formation of nanoscale Fe_3O_4 [6]. The absence of sharp peaks and the presence of a broad absorption band further confirm the nanoparticulate nature and possible polydispersity of the sample.

Elemental survey analysis: The X-ray photoelectron spectroscopy (XPS) analysis of SPR-Fe_3O_4 NPs provides insight into their elemental composition and chemical states. The survey spectrum (Fig. 6c) confirms the presence of iron (Fe), oxygen (O) and carbon (C), with no significant impurities detected, indicating high purity of the synthesized nanomaterial [18]. The high-resolution Fe 2p spectrum (Fig. 6a) shows two distinct peaks centered around 710.8 eV and 724.5 eV, corresponding to Fe $2p_{3/2}$ and Fe $2p_{1/2}$, respectively. These peaks are characteristic of iron in the Fe^{3+} oxidation state, consistent with the formation of Fe_3O_4. Moreover, a minor satellite peak is observed, further supporting the mixed valence

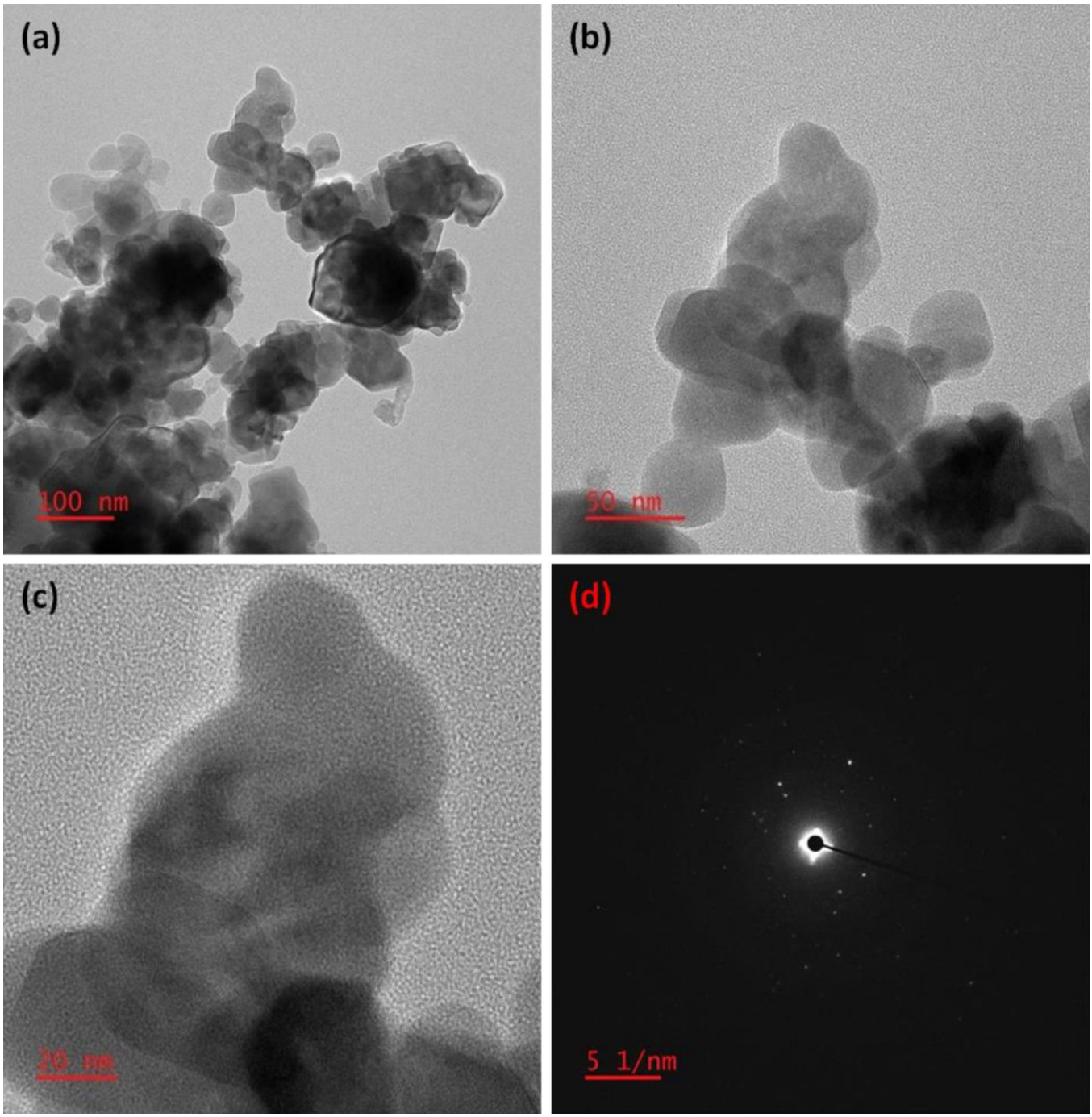

Fig. 3. TEM (a-c) and SAED (d) images of prepared SPR-Fe_3O_4 NPs

state of iron (Fe^{2+}/Fe^{3+}) typically present in magnetite. The O 1s core-level spectrum (Fig. 6b) displays a prominent peak at approximately 530.2 eV, which is attributed to lattice oxygen (O^{2-}) in the metal oxide framework. A slight shoulder at higher binding energies may suggest the presence of surface hydroxyl groups or adsorbed water, likely due to plant-based capping agents or environmental exposure.

Surface studies: The nitrogen adsorption-desorption isotherm of SPR-Fe_3O_4 NPs, as depicted in the Fig. 7, exhibits a characteristic type IV isotherm with a prominent H3-type hysteresis loop [16-18]. This behaviour is indicative of a mesoporous structure, which is typically associated with capillary condensation within slit-like pores formed by aggregates of plate-like nanoparticles. The initial linear region at low relative pressures ($P/P_o < 0.2$) suggests monolayer-multilayer adsorption, while the sharp increase in adsorbed volume at high relative pressures ($P/P_o > 0.9$) reflects the occurrence of pore filling due to mesoporous cavities. The presence of this hysteresis loop confirms the mesoporous nature of the SPR-Fe_3O_4 NPs, which is advantageous for applications such as catalysis, adsorption and drug delivery due to the enhanced surface area and accessible pore volume.

Magnetic property: The magnetic properties of SPR-Fe_3O_4 NPs were analyzed using a vibrating sample magneto-

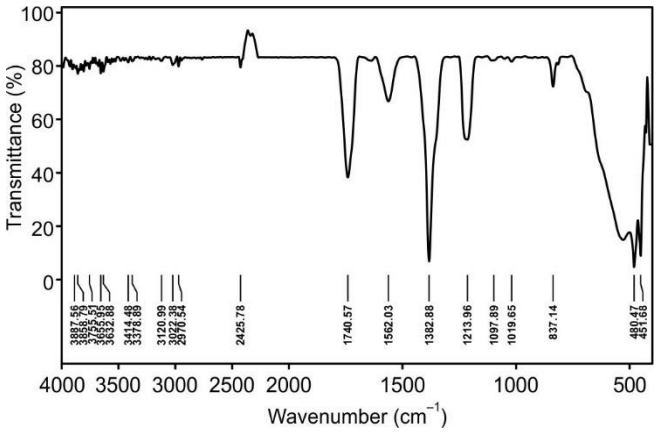

Fig. 4. FTIR spectrum of prepared SPR-Fe_3O_4 NPs

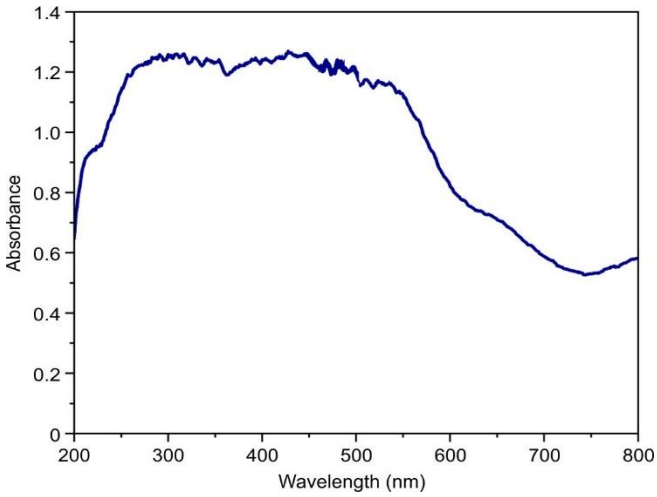

Fig. 5. UV-Vis spectrum of prepared SPR-Fe_3O_4 NPs

meter (VSM) and the resulting magnetization curve is shown in the Fig. 8. The curve exhibits a typical S-shaped hysteresis loop, characteristic of superparamagnetic behaviour. The absence of a significant coercivity (0.001 Oe) and remanence (0.0719 Oe) indicates that the nanoparticles do not retain magnetization once the external magnetic field is removed, confirming their superparamagnetic nature. The saturation magnetization value is moderate with 14999.92 Oe, suggesting effective incorporation of iron oxide with slight reduction due to the presence of organic or non-magnetic surface coatings, likely from plant-derived components used in the synthesis [16].

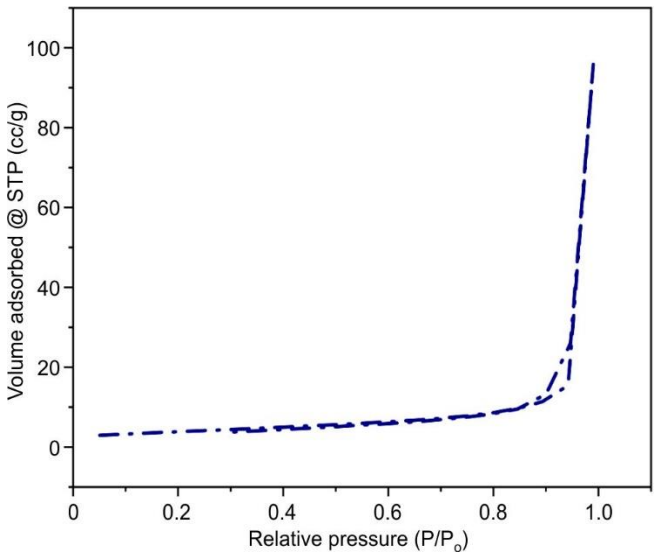

Fig. 7. N_2 adsorption isotherm

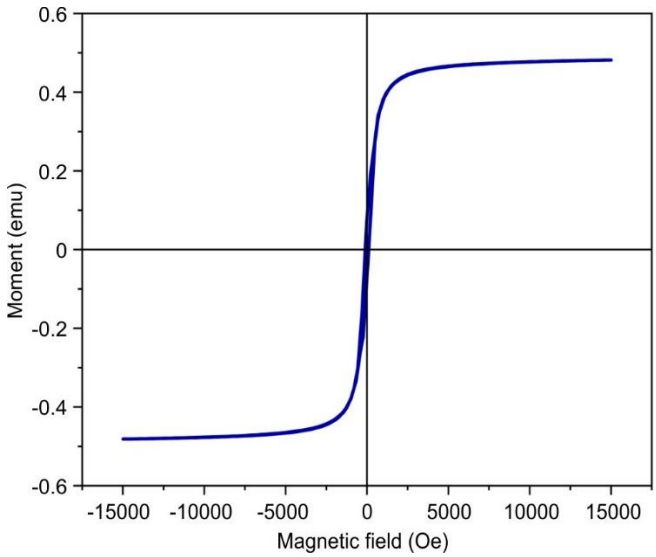

Fig. 8. Magnetic property of SPR-Fe_3O_4 NPs

Photocatalysis studies: As-characterized SPR-Fe_3O_4 NPs were further used for evaluation of photocatalytic performance towards the degradation of eosin yellow (EY) dye under visible light irradiation. The experimental conditions were setup with pH-5, 50 mg catalyst amount and 10 mg/L EY dye

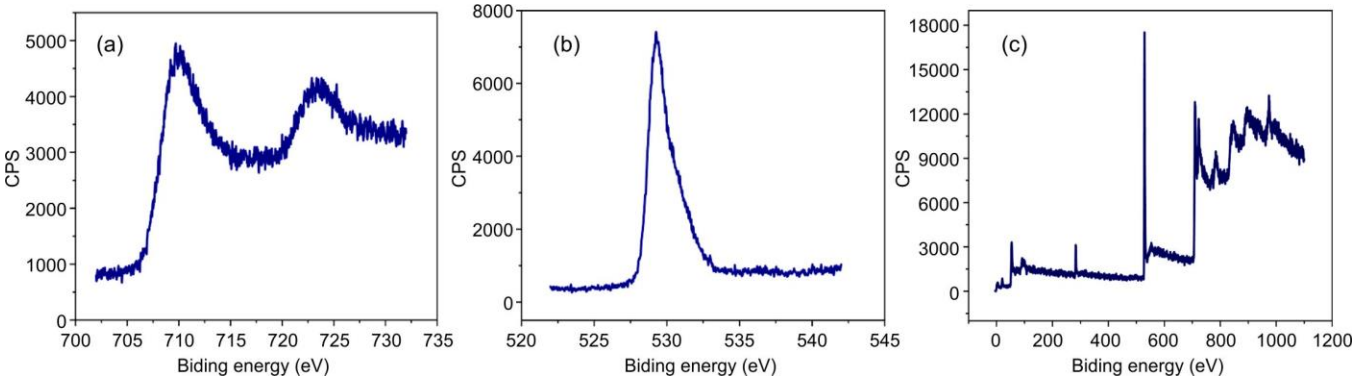

Fig. 6. XPS analysis of (a) Fe 2p, (b) O 1s and (c) survey spectrum

initial solution. The significant degradation percentage is moderate in 80 min and these results leads to do optimize the reaction conditions for obtaining complete degradation.

Optimization of pH, catalyst loading and dye initial concentrations: The degradation of eosin yellow dye was monitored using UV-visible spectroscopy by observing changes in absorbance at 517 nm under varying pH conditions (5, 7 and 9), as shown in Fig. 9a-c. A gradual decrease in absorbance intensity over time confirms the effective photocatalytic degradation of the dye. At pH 5, moderate degradation was observed with a significant reduction in absorbance after 80 min. At pH 7, enhanced degradation efficiency was noted, likely due to optimal surface charge interactions between the photocatalyst and dye molecules. Notably, at pH 9, nearly complete degradation was achieved (99.3%), indicating that alkaline conditions favour the breakdown of EY dye, possibly due to increased generation of reactive oxygen species (ROS). These results highlight the crucial influence of pH on the photocatalytic degradation process, with basic conditions proving most effective for complete dye removal.

The kinetics of EY dye degradation were investigated under varying catalyst dosages and initial dye concentrations. The plots follow pseudo-first-order kinetics, evidenced by the linear relationship between $\ln(C/C_o)$ and time. In Fig. 10a, increasing the catalyst dosage from 20 mg to 60 mg significantly enhanced the degradation rate, with 60 mg yielding the fastest reduction in dye concentration. This improvement is attributed to the greater availability of active sites and enhanced generation of reactive species. Fig. 10b shows the impact of initial dye concentration (5, 20 and 30 ppm). Lower dye concentrations favoured more efficient degradation, with the 5 ppm sample exhibiting the highest rate, complete degradation seen in 80 min. This trend can be explained by the reduced competition among dye molecules for the limited active sites on the catalyst surface [6].

Recyclability and stability: The recyclability and structural stability of the SPR-Fe_3O_4 NPs were assessed through repeated photocatalytic degradation of EY dye over five successive cycles. As shown in Fig. 11a, the catalyst retained a high degradation efficiency (> 85%) even after the 5th cycle, indicating excellent reusability with minimal activity loss. This decline is likely due to partial surface fouling or slight material loss during recovery. Fig. 11b compares the XRD patterns of the catalyst after the 1st and 5th cycles, revealing no significant shifts or changes in peak intensity or position. This confirms that the crystalline structure of SPR-Fe_3O_4 NPs remained intact, highlighting their good structural stability under repeated use.

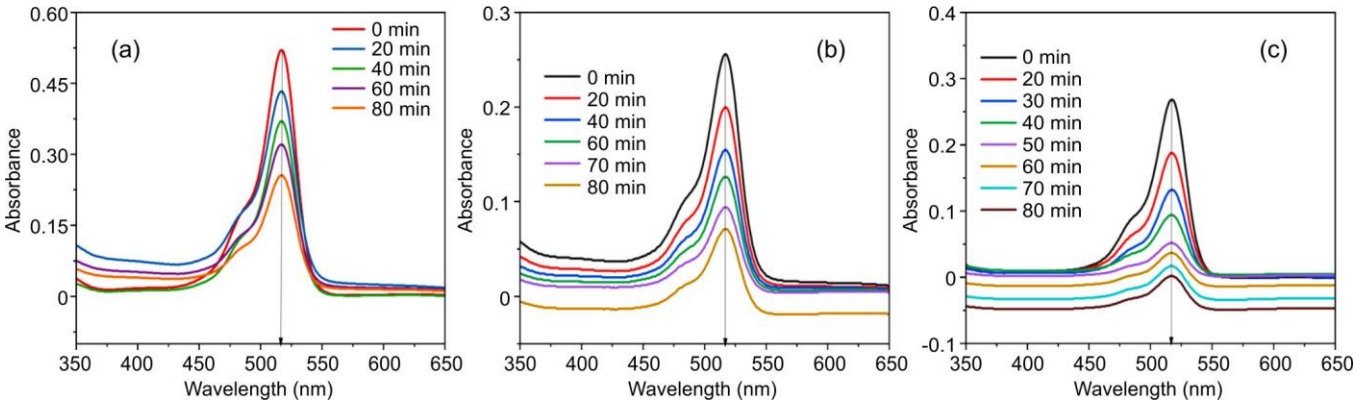

Fig. 9. EY dye degradation using SPR-Fe_3O_4 NPs at different pH (a) 5, (b) 7 and (c) 9

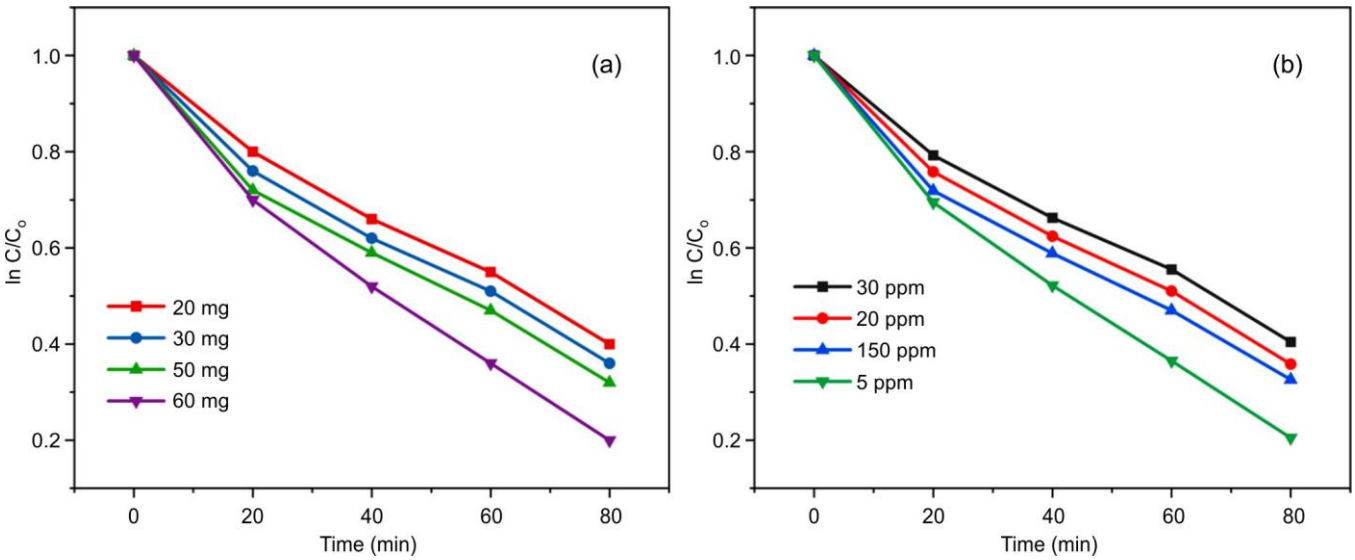

Fig. 10. Optimized conditions for EY dye degradation using SPR-Fe_3O_4 NPs (a) catalyst loading and (b) EY initial dye concentration

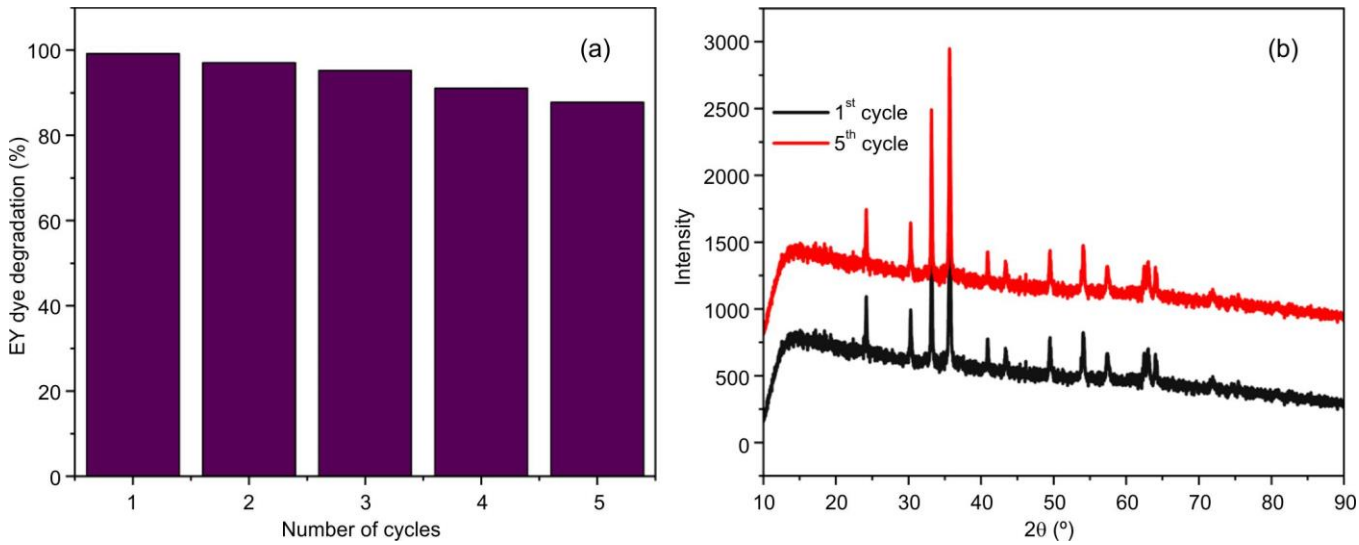

Fig. 11. EY dye degradation using SPR-Fe_3O_4 NPs (a) Recyclability and (b) sustainability

Probable mechanism: When SPR-Fe_3O_4 NPs are irradiated with visible light, their surface electrons (e^-) in the valence band (VB) absorb photon energy and get excited to the conduction band (CB), leaving behind positively charged holes (h^+) in the VB.

$$Fe_3O_4 + h\nu \text{ (visible light)} \rightarrow e^- \text{ (CB)} + h^+ \text{ (VB)} \quad (2)$$

The photogenerated electrons in the conduction band can reduce dissolved molecular oxygen (O_2) adsorbed on the nanoparticle surface to form superoxide radicals ($^{\bullet}O_2^-$).

$$e^- + O_2 \rightarrow {}^{\bullet}O_2^- \quad (3)$$

Simultaneously, the holes in the valence band can oxidize water molecules (H_2O) or hydroxide ions (OH^-) to generate hydroxyl radicals ($^{\bullet}OH$).

$$h^+ + H_2O \rightarrow {}^{\bullet}OH + H^+ \quad (4)$$

or $$h^+ + OH^- \rightarrow {}^{\bullet}OH$$

Both superoxide ($^{\bullet}O_2^-$) and hydroxyl ($^{\bullet}OH$) radicals are highly reactive oxygen species (ROS) capable of non-selectively attacking and breaking down complex dye molecules like eosin yellow (EY) into smaller, less toxic intermediates and ultimately mineralizing them into CO_2, H_2O and other harmless end products.

$$EY + {}^{\bullet}OH/{}^{\bullet}O_2^- \rightarrow \text{Degradation intermediates} \rightarrow CO_2 + H_2O + \text{Mineral acids} \quad (5)$$

Furthermore, SPR-Fe_3O_4 NPs exhibit strong magnetic properties, allowing for easy post-reaction recovery and reuse of the catalyst, while the plant-based phytochemicals possibly act as surface stabilizers, enhancing charge separation and reducing electron-hole recombination.

Anticancer activity: The cytotoxic effects of SPR-Fe_3O_4 NPs on MCF-7 breast cancer cells were evaluated by treating the cells with varying concentrations of the nanoparticles (100, 500 and 1000 μg/mL) and the cellular morphology was observed under a microscope. As shown in Fig. 12, the untreated control cells exhibit normal elongated morphology with a healthy monolayer distribution, indicating high cell viability. Upon treatment with 100 μg/mL of SPR-Fe_3O_4 NPs, minor morphological changes begin to appear, though most cells remain adherent and intact.

With increasing nanoparticle concentration to 500 μg/mL, a noticeable reduction in cell density is observed, along with signs of cellular shrinkage and rounding, suggesting early cytotoxic effects (Table-1). At the highest concentration tested (1000 μg/mL), significant morphological alterations are evident, including increased cell detachment, rounding and membrane disruption, indicating dose-dependent cytotoxicity.

These results well matched with the previous reports [19-21]. Superparamagnetic nanoparticles that exhibit ultrasmall size, uniform shape, enhanced colloidal stability, modified surface characteristics and improved magnetic response are emerging as highly suitable candidates for biomedical applications, including targeted drug delivery [19]. Several studies have demonstrated the effective loading of anticancer drugs onto magnetite nanoparticles to enhance the therapeutic efficacy of chemotherapy agents. Functionalization of Fe_3O_4 NPs with various surface modifiers such as polyethylenimine (PEI), peptides, polyvinyl alcohol (PVA), proteins and carbohydrates facilitates efficient drug encapsulation and allows controlled release [20]. One promising approach involves the

TABLE-1
ANTICANCER ACTIVITY OF SPR-Fe_3O_4 NPs ON MCF-7 BREAST CANCER CELLS

Sample conc.	Final replicate values					
	1	2	3	4	Mean	SD
0	95.14563	82.97735	111.7152	110.1618	100.0000	13.58730
100	92.94498	151.9741	131.7799	104.0777	120.1942	26.74855
500	121.6828	126.0841	117.7994	144.9838	127.6375	12.04927
1000	128.5437	126.4725	131.6505	128.0259	128.6731	2.171261

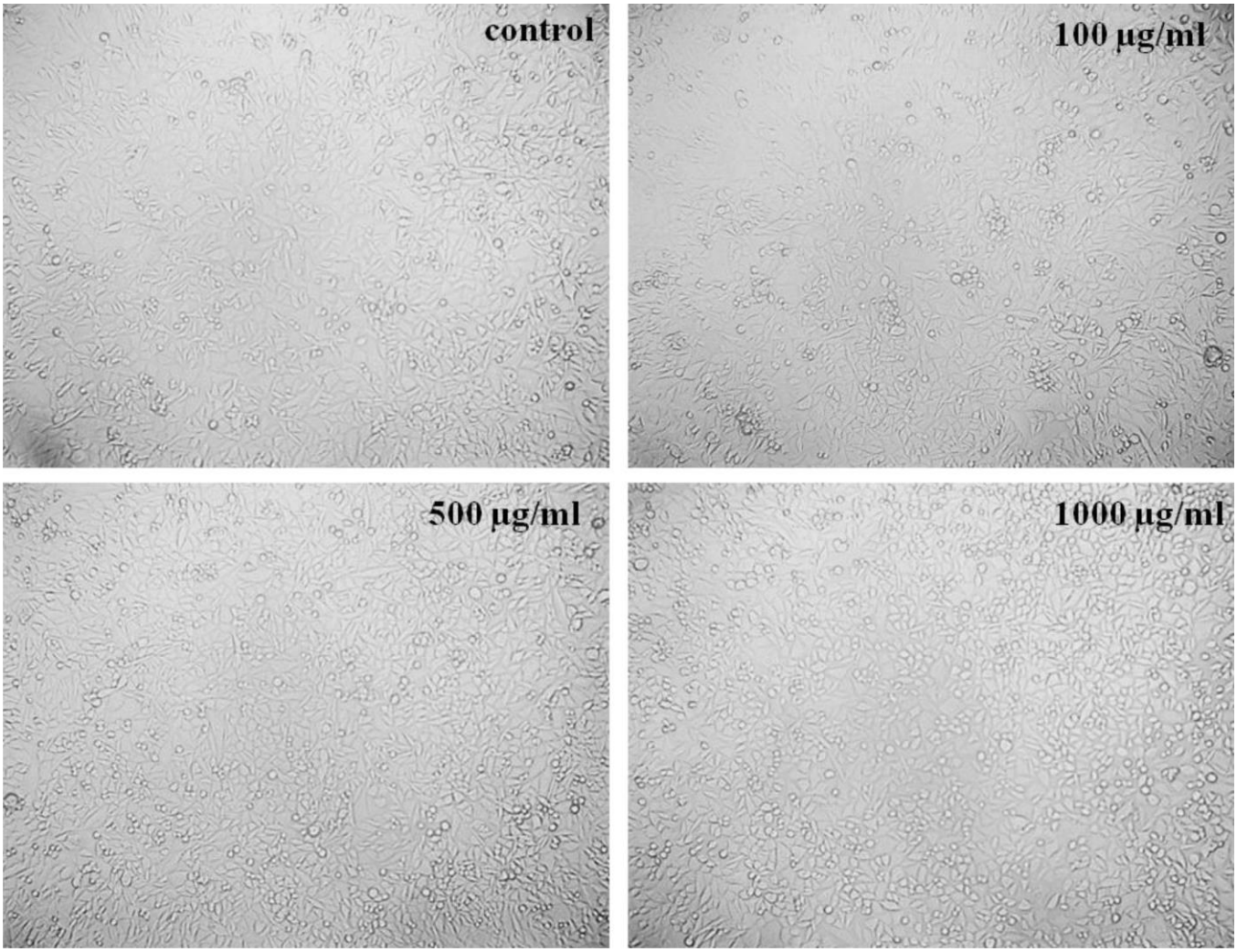

Fig. 12. Cytotoxic effects of SPR-Fe_3O_4 NPs on MCF-7 breast cancer cells

use of PEI-coated Fe_3O_4 NPs for delivering quercetin a plant-derived flavonoid known for its antiproliferative activity. This strategy not only enhances the solubility and bioavailability of quercetin but also strengthens its synergistic anticancer effect when used alongside standard chemotherapeutic drugs [21]. These results confirm that green synthesized SPR-Fe_3O_4 NPs exhibit concentration-dependent cytotoxic activity against MCF-7 cells, making them potentially useful in cancer nano-medicine applications, particularly in targeted therapy or drug delivery systems.

Conclusion

In this study, an eco-friendly synthesis of magnetically recoverable SPR-Fe_3O_4 NPs was successfully achieved using plant-based extracts. The synthesized nanocatalysts were thoroughly characterized using XRD, FTIR, SEM, HRTEM, UV-Vis and VSM analyses, confirming their structural integrity, magnetic properties and photocatalytic potential. The SPR-Fe_3O_4 NPs exhibited remarkable efficiency in the visible-light driven degradation of eosin yellow (EY) dye, demonstrating a pseudo-first-order kinetic model. Remarkably, the catalyst retained its stability and photocatalytic performance over multiple reuse cycles, highlighting its potential for practical wastewater treatment applications. SPR-Fe_3O_4 NPs exhibit concentration-dependent cytotoxic activity against MCF-7 cells effectively with significant results. The use of plant-mediated synthesis not only reduced the dependency on toxic chemicals but also offered a sustainable and cost-effective route for developing the functional nanomaterials. Overall, based on results, SPR-Fe_3O_4 NPs act as a promising, green and recyclable photocatalyst for the efficient remediation of dye-contaminated effluents and used in biomedical applications.

CONFLICT OF INTEREST

The authors declare that there is no conflict of interests regarding the publication of this article.

REFERENCES

1. B. Lellis, C.Z. Fávaro-Polonio, J.A. Pamphile and J.C. Polonio, *Biotechnol. Res. Innov.*, **3**, 275 (2019); https://doi.org/10.1016/j.biori.2019.09.001
2. C.K. Bandoh, M. Haruna, D. Adu-Poku, B.Y. Danu, O. Pinto, M. Toku, M. Badu, E.S. Agorku, F.K. Ampong and R.K. Nkum, *Discov. Appl. Sci.*, **7**, 272 (2025); https://doi.org/10.1007/s42452-025-06759-y

3. H.M. Mohammad, S.I. Saeed and L.M. Ahmed, *J. Nanostruct.*, **13**, 483 (2023); https://doi.org/10.22052/JNS.2023.02.018
4. A. Kistan, S. Narmatha, M. Chitra and L. Mayavan, *Diamond Rel. Mater.*, **151**, 111841 (2025); https://doi.org/10.1016/j.diamond.2024.111841
5. S. Bassim, A.K. Mageed, A.A. AbdulRazak and H.S. Majdi, *Inorganics*, **10**, 260 (2022); https://doi.org/10.3390/inorganics10120260
6. B.S. Mohan, K. Ravi, R.B. Anjaneyulu, G.S. Sree and K. Basavaiah, *Physica B*, **553**, 190 (2019); https://doi.org/10.1016/j.physb.2018.10.033
7. N.S. Ali, E.H. Khader, R.H. khudhur, M.A. Abdulrahman, I.K. Salih and T.M. Albayati, *Desalination Water Treat.*, **317**, 100033 (2024); https://doi.org/10.1016/j.dwt.2024.100033
8. A. Taufik, M. Muzakki and R. Saleh, *Mater. Res. Bull.*, **99**, 109 (2018); https://doi.org/10.1016/j.materresbull.2017.10.033
9. N.S. Ali, K.R. Kalash, A.N. Ahmed and T.M. Albayati, *Sci. Rep.*, **12**, 16782 (2022); https://doi.org/10.1038/s41598-022-20984-0
10. O.V. Kharissova, H.V.R. Dias, B.I. Kharisov, B.O. Pérez and V.M.J. Pérez, *Trends Biotechnol.*, **31**, 240 (2013); https://doi.org/10.1016/j.tibtech.2013.01.003
11. M.S. Mansour, Y. Farid, S.A. Nosier, O. Adli and M.H. Abdel-Aziz, *J. Photochem. Photobiol. Chem.*, **436**, 114411 (2023); https://doi.org/10.1016/j.jphotochem.2022.114411
12. F. Khan, M. Shariq, M. Asif, M.A. Siddiqui, P. Malan and F. Ahmad, *Nanomaterials*, **12**, 673 (2022); https://doi.org/10.3390/nano12040673
13. D. Adinarayana, N. Annapurna, B.S. Mohan and P. Douglas, *Desalination Water Treat.*, **320**, 100593 (2024); https://doi.org/10.1016/j.dwt.2024.100593
14. P Koteswara Rao, B.V. Babu, A. Rama Krishna, M Sushma Reddi, *J. Water Environ. Nanotechnol.*, **7**, 363 (2022); https://doi.org/10.22090/jwent.2022.04.003
15. P. Peddi, P.R. Ptsrk, N.U. Rani and S.L. Tulasi, *J. Genet. Eng. Biotechnol.*, **19**, 131 (2021); https://doi.org/10.1186/s43141-021-00229-9
16. G. Antarnusa, A. Esmawan, P.D. Jayanti, S. Rizki-Fitriani, R. Umam, A. Suherman, E. Kinarya Palupi and Ardimas, *J. Magn. Magn. Mater.*, **563**, 169903 (2022); https://doi.org/10.1016/j.jmmm.2022.169903
17. H. Kaur, A. Sharma, K. Anand, A. Panday, S. Tagotra, S. Kakran, A.K. Singh, M.W. Alam, S. Kumar, G. Bouzid, J. Dalal and G. Singh, *RSC Adv.*, **15**, 16742 (2025); https://doi.org/10.1039/D5RA01469G
18. S.M. Botsa, G.P. Naidu, M. Ravichandra, S.J. Rani, R.B. Anjaneyulu and C.V. Ramana, *J. Mater. Res. Technol.*, **9**, 12461 (2020); https://doi.org/10.1016/j.jmrt.2020.08.087
19. F. Sadeghi Nodoushan, F. Hakimian, S. Taghiyar and B.F. Haghiralsadat, *J. Nutr. Food Security*, **8**, 565 (2023).
20. R.A. Revia and M. Zhang, *Mater. Today*, **19**, 157 (2016); https://doi.org/10.1016/j.mattod.2015.08.022
21. K. Lopes, I. Cavalcante, R. Silva, D. Brito, L. Fechine, D. Moreira, ´I. Vieira, F. Azu, L. Leal, M. Ribeiro and N. Ricardo, *Quim. Nova*, **43**, 1011 (2020); https://doi.org/10.21577/0100-4042.20170570